An electrically induced probe of the modes of a plasmonic multilayer stack

Shuiyan Cao, Moustafa Achlan, Jean-François Bryche, Philippe Gogol, Gérald Dujardin, Georges Raşeev, Eric Le Moal, Elizabeth Boer-Duchemin

Research Article | Vol. 27, No. 23 / 11 November 2019 / Optics Express 33011
Optics EXPRESS

An electrically induced probe of the modes of a plasmonic multilayer stack

Shuiyan Cao,[1,2] Moustafa Achlan,[2] Jean-François Bryche,[3,4] Philippe Gogol,[3] Gérald Dujardin,[2] Georges Raşeev,[2] Eric Le Moal,[2,*] and Elizabeth Boer-Duchemin[2]

[1]*Department of Applied Physics, Nanjing University of Aeronautics and Astronautics, Nanjing, 210016, China*
[2]*Institut des Sciences Moléculaires d'Orsay (ISMO), CNRS, Univ. Paris-Sud, Université Paris-Saclay, 91405 Orsay cedex, France*
[3]*Centre de Nanosciences et de Nanotechnologies (C2N), CNRS, Univ. Paris-Sud, Université Paris-Saclay, 91120 Palaiseau, France*
[4]*Laboratoire Nanotechnologies et Nanosystèmes (LN2) - CNRS, Université de Sherbrooke, J1K 0A5 Sherbrooke, Canada*
[*]*eric.le-moal@u-psud.fr*

Abstract: A new single-image acquisition technique for the determination of the dispersion relation of the propagating modes of a plasmonic multilayer stack is introduced. This technique is based on an electrically-driven, spectrally broad excitation source which is nanoscale in size: the inelastic electron tunnel current between the tip of a scanning tunneling microscope (STM) and the sample. The resulting light from the excited modes of the system is collected in transmission using a microscope objective. The energy-momentum dispersion relation of the excited optical modes is then determined from the angle-resolved optical spectrum of the collected light. Experimental and theoretical results are obtained for metal-insulator-metal (MIM) stacks consisting of a silicon oxide layer (70, 190 or 310 nm thick) between two gold films (each with a thickness of 30 nm). The broadband characterization of hybrid plasmonic-photonic transverse magnetic (TM) modes involved in an avoided crossing is demonstrated and the advantages of this new technique over optical reflectivity measurements are evaluated.

1. Introduction

Stacking dielectric and metallic layers one on top of another is an extremely versatile way to create systems that have novel functionalities since such structures support new kinds of optical modes. Applications of such stacks in biosensing [1], superlensing [2,3], radiative decay engineering [4], waveguiding [5,6] and tunable light sources [7,8] have been reported. In this context, a simple technique that can be used to obtain the dispersion relation of the optical modes of such systems is indispensable.

In principle, the energy-momentum dispersion relation of the modes of the system that couple to light may be retrieved from optical reflectivity measurements, e.g., using plane-wave illumination through a prism in a Kretschmann-Raether (KR) configuration [9]. However, prism-based KR experiments generally require sweeping the incidence angle and beam wavelength over a wide range of values—a single-shot, broadband measurement, on the other hand, would be more practical. This, however, is not possible in a standard prism-based KR experiment. In theory, such a measurement may be carried out by simultaneously illuminating the sample at all angles using a *focused* white light source [10]. In practice, however, tightly focusing a spectrally broad beam of light is difficult due to the inherent abberations of high numerical-aperture lens systems [11]. Nonetheless, such issues may be overcome through the use of a *local* source, in which case both the spatial extent and the power spectrum of the excitation may be controlled.

#376418 https://doi.org/10.1364/OE.27.033011
Journal © 2019 Received 27 Aug 2019; revised 18 Oct 2019; accepted 22 Oct 2019; published 28 Oct 2019

Optics EXPRESS

Various different strategies have been used to obtain a local source of light, e.g., the use of an optical fiber or a scattering tip in a scanning nearfield optical microscope [12–16], sometimes in combination with a plasmonic or photoluminescent nanoparticle [17–20]. Nevertheless, the excitation spectrum of these techniques is often narrow compared to the frequency range of interest (the visible and near infrared) for most studies of plasmonic systems. On the other hand, the truely local and spectrally broad excitation of optical modes is possible using the high-energy (~30 keV) electron beam of a scanning [21] or transmission [22] electron microscope. In this case, the electron-matter interactions produce light via cathodoluminescence [23]. Among other studies, this approach has been used to investigate the optical modes of plasmonic multilayer stacks [7,24,25]. The main drawback of these excitation techniques is the vacuum environment and associated cost of the necessary *high energy* electrons.

In contrast, inelastic electron tunneling (IET) through a nanometer-scale tunnel junction provides a spectrally broad excitation source using *low energy* electrons [26,27]. Advantageously, this approach is compatible with ambient conditions, uses low voltage and low current, and can be implemented using a scanning tunneling microscope (STM) operating in air [28–30]. The spatial selectivity of the electrical excitation of optical modes with an STM tip is well beyond the diffraction limit of light [31]. On the scale of visible wavelengths, the excitation source may indeed be considered a point-like electric dipole [32–34]. The emission of this point source continuously ranges from the infrared to visible frequencies and the power spectrum of the excitation source is determined by the probability of inelastic tunneling, the applied voltage and the optical response of the tip-surface nanocavity [29,32]. When a non-plasmonic tip is used, as is the case here where we use a tungsten tip, it has been shown that the presence of the tip does not disturb the native modes of the sample, since no sharp tip-surface nanocavity resonances are present [34].

Over the last decade, the combination of ambient STM with optical microscopy has been increasingly applied to experiments in nano-optics [28–31,33–45]. Most recently, this technique has been used to study the propagation of surface plasmon polaritons (SPPs) in 2D plasmonic crystals [43] and the spectral response of plasmonic lenses [44]; however, the measurement of the dispersion relation of the optical modes in a plasmonic system using this technique has never been reported before.

In this article, we show that an "STM-nanosource" coupled to an optical microscope may be used to measure the dispersion relation of the propagating modes in a plasmonic multilayer stack. The STM-nanosource results are compared to optical reflectivity measurements (acquired using a focused laser beam) and to theoretical calculations of the energy-momentum dispersion relations. In this way we demonstrate that only a *single* image is required for the broadband characterization of the hybrid plasmonic-photonic TM modes of a metal-insulator-metal stack.

2. Methods

2.1. Experimental setup

Figure 1 shows schematically the different excitation and detection configurations used in this study. All experiments are carried out using an inverted optical microscope (Nikon Instruments, Eclipse Ti-U) equipped with an oil-immersion, high numerical aperture (NA= 1.49), 100× objective lens (Nikon CFI Apochromat TIRF objective). The microscope is coupled to a cooled CCD camera (Andor, IKON-M) and an imaging spectrometer (Horiba Jobin Yvon, IHR320 spectrometer and Synapse CCD detector). A pair of achromatic doublet lenses arranged in a telescope configuration is used to image the back focal plane of the microscope objective on the CCD detector. The resulting Fourier-space image reveals the angular distribution of the collected light, which is related to the wavevectors of the excited propagating waves in the sample. Using a removable mirror, the Fourier-space image may be projected onto the entrance slit of the imaging spectrometer. Thus, an image with angular (or wavevector) coordinates along one axis

Optics EXPRESS

and wavelength (or energy) coordinates along another is measured. From such a measurement, the energy-momentum dispersion of the excited modes may be retrieved.

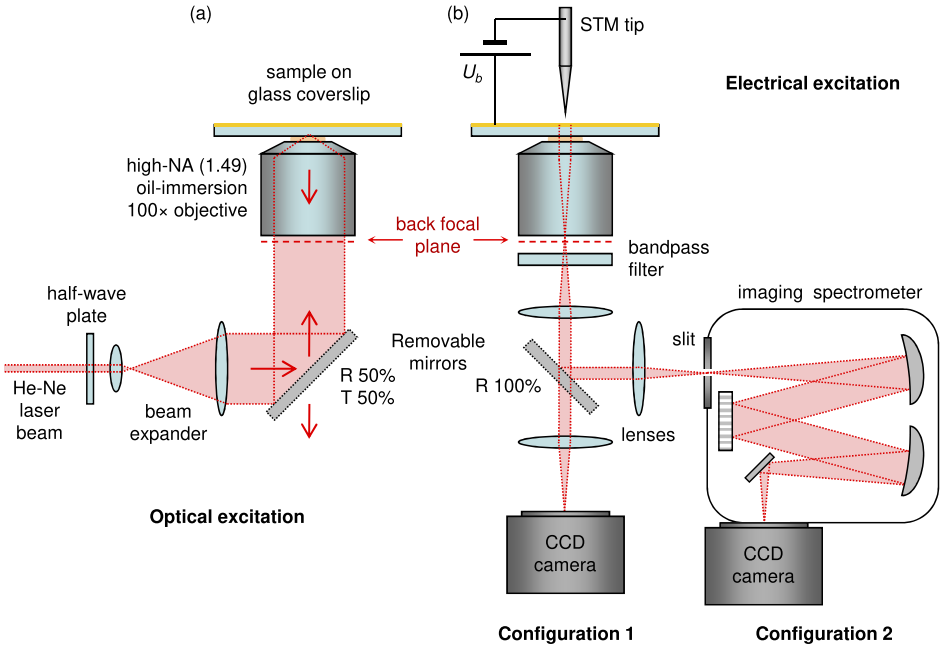

Fig. 1. Schematics of the experimental setup. (a) Optical excitation and (b) electrical excitation.

The configuration shown in Fig. 1(b) is used for the *electrical* excitation of the sample with tunnel electrons. A commercial STM head (JPK Nanowizard III) is mounted on the inverted optical microscope, so that the sample is between the objective lens and the STM tip [44]. The inelastic electron tunnel current from the tip to the surface excites both the plasmonic and photonic modes in the sample. These modes then propagate away from the tip [28,30]. On a planar metallic surface, this excitation may be considered equivalent to an oscillating electric dipole located in the tip-surface gap and oriented orthogonally to the metallic surface [29,32]. The electrically excited waves that propagate along the surface may be detected when they leak in the substrate at angles within the acceptance cone of the microscope objective [12,46].

The configuration shown in Fig. 1(a) is designed for the *optical* excitation of the sample, i.e., with a laser. The microscope objective is used both to focus the beam of a continuous-wave He-Ne laser (λ_0 = 632.8 nm) onto the substrate-sample interface and also to collect the reflected light. The laser beam is expanded using a telescope configuration to completely fill the rear pupil of the microscope objective. Thus, the reflectivity of the substrate-sample interface is measured at all incident angles within the acceptance cone of the objective in a single Fourier-space image. Moreover, since the initial beam is linearly polarized, the focused incident light is *s*-polarized in one plane and *p*-polarized in a perpendicular plane. In this way, the reflectivity for both *s*- and *p*-polarized incidence are measured simultaneously [47].

2.2. Sample fabrication

The samples are metal-insulator-metal (MIM) stacks consisting of a silicon oxide layer between two gold films. This specific geometry is an excellent prototype for the demonstration of our technique. The number and dispersion relations of the optical modes in such MIM systems may be controlled by varying a single parameter, the thickness of the insulating layer between the two

Optics EXPRESS

metallic films. Moreover, a plasmonic MIM with a very similar structure was recently proposed as a novel type of SPR sensor with enhanced detection sensitivity [1].

The MIM stacks are deposited on standard glass microscope coverslips. The two 30-nm-thick gold films are obtained by e-beam evaporation in vacuum. A 2-nm-thick titanium layer is first deposited on the glass in order to improve adhesion of the gold to the substrate. No additional adhesion layers are used at the gold-silicon oxide interfaces in order to avoid supplementary optical losses. The silicon oxide layer is grown by RF sputtering deposition in a mixed argon/oxygen atmosphere (67%/12%). Samples with silicon oxide thicknesses of 70 nm, 190 nm and 310 nm are studied. The thickness and permittivity of each layer in the stack is measured by ellipsometry. The gold layer thickness of 30 nm was chosen in order to optimize the transmitted flux from the modes of the MIM system, as based on preliminary calculations.

2.3. Theoretical calculations

The theoretical calculations are carried out using an analytical model, the details of which are provided in the Appendices. Briefly, the electrical excitation of the existing optical modes through inelastic electron tunneling between the tip and the sample is modeled using a point-like oscillating electric dipole located in the tip-sample gap. The oscillating dipole is orthogonal to the sample surface (see Appendix A) restricting the light emission to the *p* polarization. Figure 2(a) shows a schematic of the modeled system. The spherical-wave emission from the vertical dipole is expressed in terms of a continuous sum of plane waves using the Sommerfeld expansion (see Refs. [48–50]). Then, the Poynting vector or energy flux per unit time and per unit area of the emitted light through the multilayer stack is expressed in terms of the Fresnel transmission

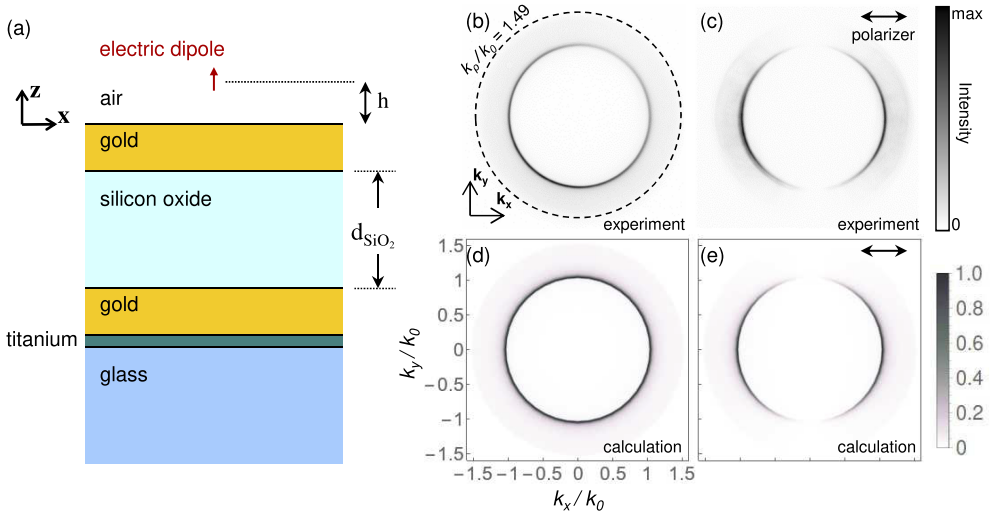

Fig. 2. Electrical excitation of a MIM stack: theory and experiment. (a) Schematic of the modeled system (not to scale). A vertical oscillating electric dipole is located at a distance h = 1 nm above a MIM stack. The stack consists of a silicon oxide layer of thickness d_{SiO_2} sandwiched between two 30 nm-thick gold layers on a glass substrate. A 2-nm-thick titanium layer is used to increase the adhesion of the gold to the glass. [(b),(c)] Experimental Fourier-space images measured upon STM excitation of an Au-SiO_2-Au MIM system with d_{SiO_2} = 310 nm (acquisition time 300 s, sample bias 2.8 V, setpoint current 1 nA). In (c), a polarizer is set in front of the CCD camera with its transmission axis along $\mathbf{k_x}$. The corresponding theoretical Fourier-space images for parts (b) and (c) are shown in parts (d) and (e) respectively. In the simulations, the spectrally broad excitation has a flat power spectrum ranging in wavelength from λ_0 = 400 to 1000 nm.

Optics EXPRESS

coefficients of the entire stack, which are calculated using Abèles transfer matrix algorithm in Bethune's implementation [51] (see Appendix B). The dispersion graphs are calculated by representing the intensity of the transmitted flux of the electromagnetic wave on a grid of the real in-plane wavevector k_ρ/k_0 and of the energy $\hbar\omega$. Finally, the nature of the excited optical modes is inferred from the electric field profile along the direction orthogonal to the stacks. This last result is obtained using Bethune's transfer matrix algorithm (see Appendix C).

3. Results

3.1. Electrical excitation

In a system such as a MIM stack, the different optical modes that exist are expected to have a specific energy-wavevector relation, i.e., a mode of a certain energy will have a particular wavevector. Since the optical Fourier space corresponds to "k-vector" or "wavevector" space, a Fourier-space image of the emission from the excited modes will give information on their wavevector distribution. Figure 2(b) shows an experimental Fourier-space image recorded upon STM excitation of an Au-SiO_2-Au MIM stack with oxide thickness d_{SiO_2} = 310 nm. "Configuration 1" of the experimental setup introduced in Fig. 1(b) is used. The detected light is not spectrally filtered, i.e., the signal is integrated over the broad power spectrum of the excitation source, weighted by the detection efficiency of the instrument. Due to the symmetry of the excitation and of the system, the resulting image is seen to be independent of direction in the k_x/k_y-plane, indicating that the STM locally excites out-going circular waves in the MIM stack which propagate isotropically away from the tunnel junction. In Fig. 2(c), a polarizer is set in front of the CCD camera with its transmission axis parallel to the **x**-axis. The total extinction of the transmitted light along the $\mathbf{k_y}$-axis demonstrates that the emitted light is purely *p*-polarized (i.e., TM or radially polarized). Simulations of the corresponding Fourier-space images, calculated using the model described in Sec. 2.3, are shown in Figs. 2(d) and 2(e), respectively. In both the experimental and calculated images, a sharp ring of radius $k_\rho/k_0 = 1.03$ and a comparatively fainter and broader ring that extends from $k_\rho/k_0 = 1$ to the collection limit of the microscope objective (i.e., $k_\rho/k_0 = 1.49$), are seen. Such rings are the result of the excitation of the optical modes of the MIM stack. These modes may be plasmonic or photonic, or a hybridization of the two. A step towards identifying the nature of the excited modes is to determine the energy-wavevector (or energy-momentum dispersion) relations. While this could be carried out by repeating the above "configuration 1" experiment with different filters in front of the detector, a more efficient one-shot measurement is performed using "configuration 2" of the set-up presented in Fig. 1(b).

3.2. Energy-momentum dispersion relation

Figures 3(a)–3(c) show the experimental dispersion relations obtained from angle-resolved optical spectra measured upon STM excitation of the different MIM stacks with oxide thicknesses of d_{SiO_2} = 70, 190 and 310 nm acquired using "configuration 2" of Fig. 1(b). To obtain this data, the Fourier-space image is projected onto the entrance slit of the imaging spectrometer using lenses, so that the $\mathbf{k_y}$-axis is parallel to the slit and the origin of Fourier space, i.e., $(k_x,\ k_y) = (0, 0)$, is in the center of the slit. Thus, the slit selects a narrow band of light along the $\mathbf{k_y}$-axis, i.e., a narrow k_x-range around $k_x = 0$. This light is then dispersed in energy by the diffraction grating of the spectrometer. In this way, the energy-momentum dispersion relations of the excited waves along $\mathbf{k_y}$ is recorded in a single image on the CCD camera of the spectrometer. Since the MIM stacks are isotropic in the plane of the layers, the dispersion along $\mathbf{k_y}$ contains all the information about the energy-momentum dispersion relations of the propagating modes that couple to light (for the investigated spectral range). Obtaining the dispersion relation from a *single* image is only possible since the excitation source is spectrally broad and isotropic in the *xy*-plane.

Optics EXPRESS

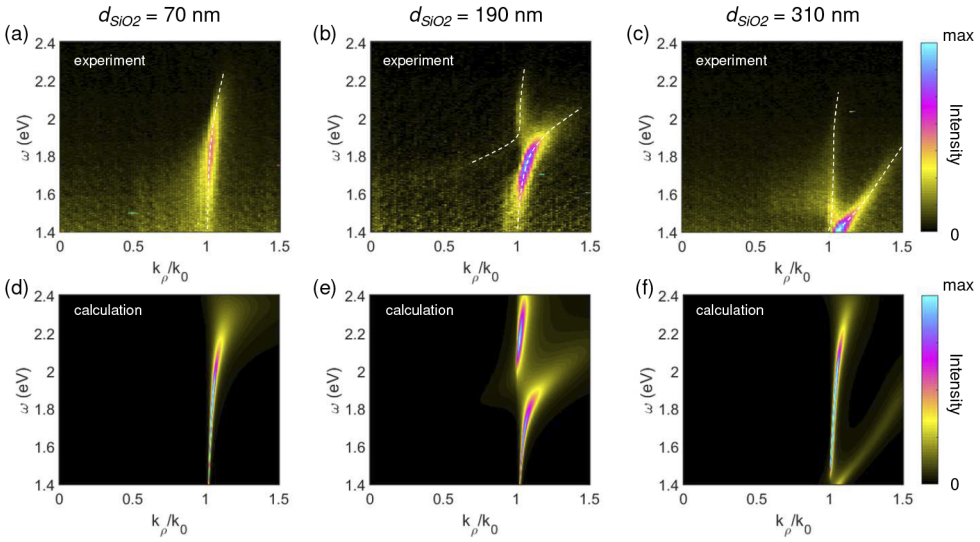

Fig. 3. Dispersion relations of the propagating modes in three MIM stacks as obtained by electrical excitation. [(a)–(c)] Experimental dispersion relations measured upon STM excitation of Au-SiO_2-Au MIM stacks with SiO_2 layer thicknesses of (a) 70 nm, (b) 190 nm and (c) 310 nm (acquisition time 300 s, sample bias 2.8 V, setpoint current 1 nA). The white dashed lines are freehand curves added to guide the eye along the maxima of the intensity plot. [(d)–(f)] Theoretical dispersion calculations of the transmitted photon flux for the same MIM stacks as in the experiment. On the horizontal axis, $k_\rho/k_0 = n_{glass} \sin\theta$ where k_ρ is the in-plane wavevector component, k_0 equals ω/c, n_{glass} is the refractive index of glass and θ is the detection angle in glass. The experimental data in wavelength has been converted to energy using a Jacobian transformation [52,53].

In Fig. 3(a) (MIM stack with d_{SiO_2} = 70 nm), a single optical band is observed in the angle-resolved spectrum. Such a curve is reminiscent of the dispersion curve for SPPs propagating on an air-gold interface of a single gold film on glass. Note that any mode that might exist but whose effective index (k_ρ/k_0, where k_ρ is the in-plane wavevector component and k_0 equals ω/c) is greater than the refractive index of the glass substrate will not be detected.

When the silicon dioxide layer thickness is increased [d_{SiO_2} = 190 and 310 nm, in Figs. 3(b) and 3(c)], *two* branches in the dispersion curve are observed. The energy at which this splitting occurs is 1.96 eV for d_{SiO_2} = 190 nm and 1.40 eV for d_{SiO_2} = 310 nm. More importantly, the evolution of each branch (or mode) as a function of effective index is seen to be very different: in one case the curve is practically vertical on the graph, corresponding to a mode with little dispersion (i.e., weak energy dependence of the mode effective index on energy), while in the other, the dispersion is significant (the dependence of the mode effective index on energy may not be ignored). Such dispersion relations are typical of *SPP* and *waveguided* (WG) photonic modes, respectively.

Though difficult to see in the experimental images, a minimum in the mode density between the two observed branches in Figs. 3(b) and 3(c) would suggest that the two observed modes are approaching a strong coupling regime, giving rise to an avoided crossing of the dispersion curves and a shift in energy (or Rabi splitting) of the modes at resonance [54]. This is more clearly visible in the simulations (obtained using the model of Sec. 2.3), as seen in Fig. 3(e) and 3(f). Indeed, in the simulations, which exhibit good qualitative agreement with experiment, the drop in mode density (energy gap opening) and the associated avoided crossing of the SPP and WG photonic bands are evident. A Rabi splitting energy of about 0.50 eV is estimated

Optics EXPRESS

from the calculated image of Fig. 3(e). In the experimental data [Fig. 3(b)], a lower value of the Rabi splitting is estimated (about 0.33 eV), and the optical bands are comparatively broader, presumably due to losses from surface roughness and inexact values for the permittivity of gold and titanium.

3.3. Mode analysis

In order to determine the nature of the excited modes, the electric field in the different layers of the sample may be calculated [4,55–58]. This is carried out theoretically by illuminating the structure with a plane wave from the glass substrate (see Appendix C for details). Figure 4 shows the z-dependence of the electric field modulus as a function of energy for different values of the in-plane wavevector component k_ρ/k_0.

At a value of k_ρ/k_0 just below that of an SPP-mode on an air/gold interface [see Fig. 4(a) and (b)], a single mode is present. The presence of significant electric field in both the air and SiO_2 layers demonstrates that the mode is a hybridized SPP/photonic waveguide mode. With the particularly strong electric field in air, especially for the stack with the thicker SiO_2 layer [part (b)], we can conclude that this mode is of dominantly SPP character.

For a value of k_ρ/k_0 just above that of an SPP-mode on an air/gold interface [see Fig. 4(c) and (d)], two modes are found. These modes are of the same character as previously. As k_ρ/k_0 is increased further, however, [see Fig. 4(e) and (f)], the field in the SiO_2 layer increases relative to that in air. In other words, as would be expected, as k_ρ/k_0 becomes significantly larger than that of an SPP-mode on an air/gold interface, the waveguide character of the hybrid mode increases. Indeed, the photonic waveguide mode dominates for the highest values of k_ρ/k_0 shown in Fig. 4(g) and Fig. 4(h).

3.4. Optical versus electrical excitation

Figures 5(a) and 5(d) show experimental Fourier-space images obtained while illuminating the sample from below with a focused laser beam (λ_0 = 632.8 nm) using the experimental set-up of Fig. 1(a). The incident electric field is linearly polarized along the **x**-axis as shown by the double arrow on the top righthand corner of the image. For a MIM sample in this configuration, the incident light is only weakly transmitted and is instead mainly reflected, except for the case where the incident angle and polarization permit the excitation of the optical modes in the sample. This excitation of the optical modes produces dark areas in Fourier-space images acquired in reflection such as those in Figs. 5(a) and 5(d). Here, the MIM stacks with d_{SiO_2} = 190 and 310 nm are investigated. Experimental Fourier-space images recorded upon STM excitation of the same two MIM stacks are shown in Figs. 5(b) and 5(e). The same experimental configuration as in Fig. 2(b) is used; however, in order to compare the optical and electrical excitation of the MIM stacks using similar spectral ranges, a bandpass filter transmitting light at 625 nm with a bandwidth of 26 nm is set in front of the CCD camera. Note that the STM-nanosource Fourier-space images are displayed using a reversed intensity scale (i.e., the darker the color, the more intense the emitted light), so that the optical modes stand out against a bright background in all cases.

Two main differences may be easily observed when the Fourier-space images obtained under optical and electrical excitation are compared (Fig. 5). The first is the fact that while complete rings are observed in the STM-excitation images, only partial arcs are present in the case where the sample is illuminated by a focused laser beam. The second is that while the same rings or arcs appear in the $\mathbf{k_x}$-axis direction for both types of excitation (labels 1 and 2), the rings or arcs in the $\mathbf{k_y}$-axis direction do not correspond (i.e., they are located at different values of k_y, see arcs with the label 3). This analysis is confirmed by the intensity cross-sections of Figs. 5(c) and 5(f). These results may be understood by recalling that since the incident laser beam is linearly polarized, the incident illumination is s-polarized in one plane and p-polarized in the other when it is focused on the sample surface. As shown in Fig. 2(c), the STM-nanosource

Optics EXPRESS

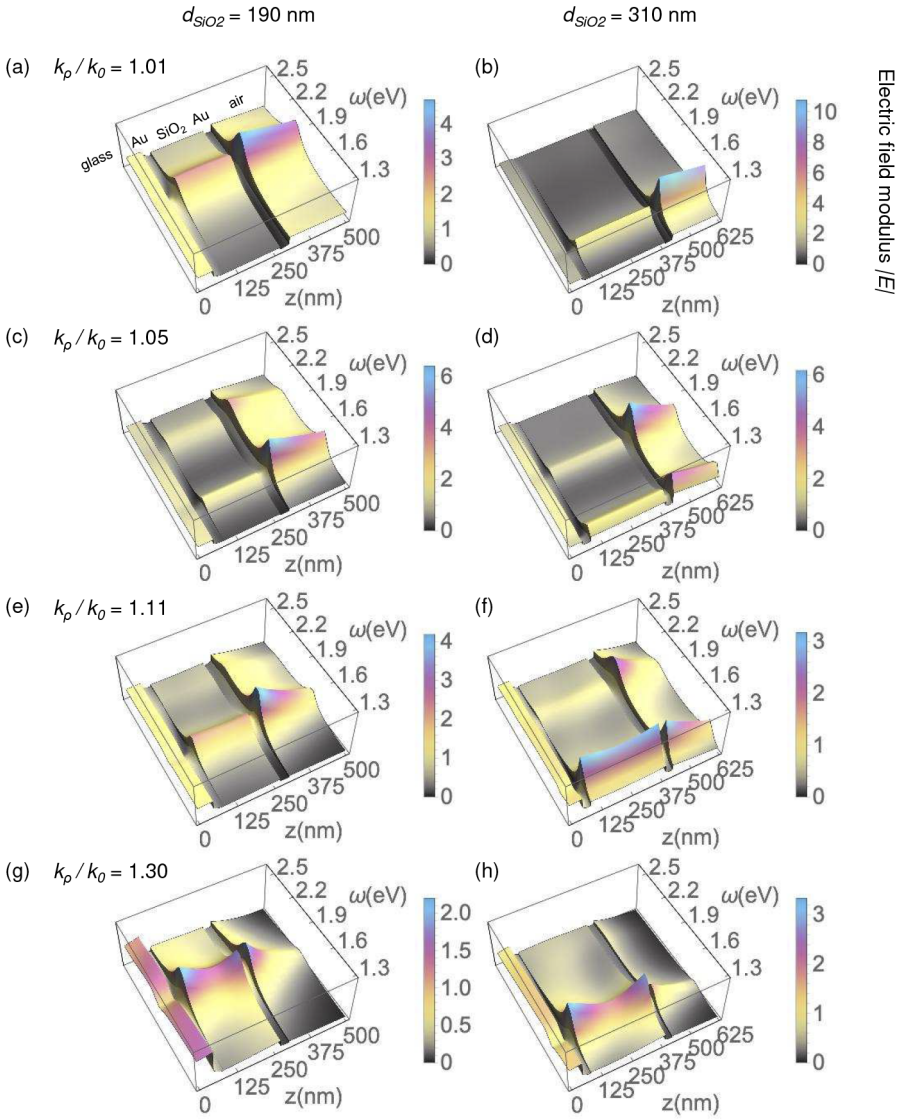

Fig. 4. Theoretical calculations of the modulus of the electric field in MIM stacks as a function of z (spatial coordinate in the direction perpendicular to the stack layers) and energy, for different values of the in-plane wavevector k_ρ/k_0. SiO_2 layer thicknesses of 190 nm and 310 nm are considered (see left and right columns respectively). The k_ρ/k_0 values used are (a)–(b) 1.01, (c)–(d) 1.05, (e)–(f) 1.11 and (g)–(h) 1.30.

excites *p*-polarized or transverse magnetic (TM) modes. This is confirmed when taking into account that the experimental laser polarization is such that the incident light is *p*-polarized in the x direction – indeed, along $\mathbf{k_x}$, the optical and electrical excitation results are equivalent. In the $\mathbf{k_y}$-axis direction, the incident illumination is *s*-polarized: we may thus conclude that the modes present in the optically excited image along the $\mathbf{k_y}$-axis are *s*-polarized or transverse electric (TE) modes. Note that these TE modes may not be excited by the STM-nanosource, which may be considered as a vertical oscillating electric dipole.

Optics EXPRESS

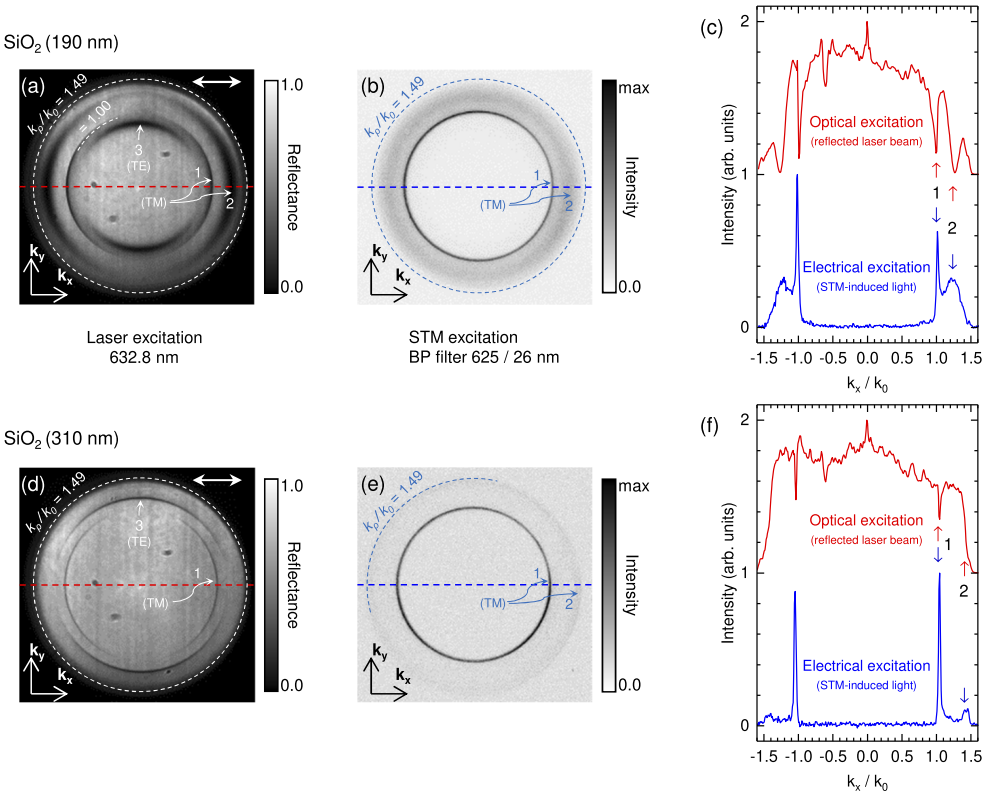

Fig. 5. Comparison of optical and electrical excitation. The experimental data is measured on the Au-SiO_2-Au MIM stacks with (a)–(c) d_{SiO_2} = 190 nm and (d)–(f) d_{SiO_2} = 310 nm. Parts (a) and (d): Fourier-space images acquired in reflection when the sample is back-illuminated with a focused laser beam emitting at λ_0 = 632.8 nm. Parts (b) and (e): Fourier-space images acquired using STM excitation of the sample; a bandpass filter centered at λ_0 = 625 nm with a bandwidth of 26 nm is placed before the detector (acquisition time 300 s, sample bias 2.8 V, setpoint current 1 nA). [(c) and (f)] Intensity profiles taken along the $\mathbf{k_x}$-axis (dashed lines) in the Fourier-space images shown in (a), (b), (d) and (e), respectively. In (a) and (d), a spinning diffuser is placed in front of the laser source to reduce the speckle of the laser beam in the recorded reflection images.

For the MIM stack with d_{SiO_2} = 190 nm, the signature of the detected TE mode lies within the subcritical angular range. Thus the incident light is transmitted through the MIM stack and propagates away in the air above the sample. The drop in reflectance may thus be understood as a transmission resonance of the MIM stack (such as in a Fabry-Perot resonator) and the radial width of the dark arcs in Fourier space is determined by the reflection coefficients at the gold-silicon oxide interfaces. For the MIM stack with d_{SiO_2} = 310 nm, however, the reflectance dip of the TE mode occurs at a supercritical angle and its radial width is comparatively narrow. This excited TE mode must be an optical waveguide mode that propagates in the plane of the MIM stack.

Note that in general, the detection of emitted light over a dark background generally results in more sensitive measurements than the detection of the absorption of light (i.e., the inverse contrast) in a bright field. This is because of the difficulty of illuminating the sample with a spatially and spectrally homogeneous optical field. As seen in Figs. 5(a) and 5(d), the inhomogeneous illumination pattern (despite the use of a spinning diffuser in front of the laser source) complicates the distinction between artifactual and real features and the quantitative measurement of the

Optics EXPRESS

reflectivity variations; in comparison, the baseline of the electrically excited light is flat. Thus, with electrical excitation, even comparatively faint features occurring at high angles close to the maximum acceptance angle of the microscope objective (i.e., where the objective's transmission drops) may be detected. For instance, the peak/dip at $k_\rho/k_0 = 1.45$ (the objective's NA is 1.49) in Fig. 5(f) is identified with difficulty in the reflected light data, whereas it clearly distinguishes itself from the background in the STM-induced light data [see the arrow numbered 2 in Fig. 5(e)]. In addition, recent theoretical work [59–62] has shown that *reflectivity* measurements in the Kretschmann configuration may be less accurate for the determination of the dispersion relations of the propagating modes in plasmonic stacks than techniques based on the *leakage radiation* of the excited modes such as the STM-technique described above.

Nonetheless, the STM-based technique used in this study also has several drawbacks as compared to far-field and near-field optical techniques. On a flat horizontal surface, the excitation source resulting from the inelastic tunnel current flowing between the tip and the surface invariably behaves like a vertical oscillating electric dipole. As a result, only TM optical modes of the sample may be excited (i.e., TE modes may not be detected). It may, however, be possible to overcome this difficulty via the functionalization of the tip with a plasmonic nanoparticle in such a way that a tilted electric dipole may be generated [31,34]. Such an excitation could then couple to both TE and TM modes. In addition, the flux of emitted photons is fundamentally limited by the electronic current passing through the junction in the tunneling regime (in the nA range) and the electron-to-optical mode conversion efficiency (theoretically in the $10^{-6} - 10^{-4}$ range [32]). On average, this yields photon fluxes at the detector in the range of 10^3 to $10^5 s^{-1}$. Therefore, exposure times of several minutes are often necessary to record typical values of $100 - 1000$ counts per pixel of the CCD camera. Here also, a solution may be found in the use of a specific tip design, e.g., a plasmonic tip engineered in a way so as to increase the local density of modes inside the tip-sample gap [63].

4. Conclusion

To conclude, the inelastic electron tunnel current from the tip of an STM provides an extremely local and spectrally broad excitation source which may be used to probe the density of optical modes in a plasmonic multilayer stack, e.g., a metal-insulator-metal or MIM sample. The energy-momentum dispersion relations of the propagating modes is determined from the angle-resolved optical spectrum in transmission. This transmitted flux is measured using an optical microscope and an imaging spectrometer coupled to the STM head. Thus, the hybrid plasmonic-photonic TM modes of a sample may be characterized from a single image. This approach may naturally be extended to the measurement of the *optical band structure* in systems exhibiting spatial periodicity in the lateral direction, i.e., plasmonic and photonic crystals and metasurfaces.

The STM-based technique introduced here has several advantages over existing far-field and near-field optical characterization methods. Its true deep-subwavelength spatial selectivity and its ability to provide STM topography images with nanoscale spatial resolution are strong assets for the study of nanostructured or surface-functionalized systems. In principle our technique is fully compatible with STM at the liquid-solid interface, where submolecular resolution may be attained even at room temperature (see, for example [64]). In addition, our excitation source has a broader power spectrum than most optical probes based on a quantum nanoemitter (e.g., a semiconductor nanocrystal or an NV center in a nanodiamond), without resorting to the use of a tunable or supercontinuum laser source as in, for example, previous aperture near-field optical microscopy studies [65,66]. In principle, the spectral distribution of the excitation source is only limited in energy by the applied bias voltage [26], which makes it well suited for studies in the near infrared [67]. Moreover, the well-controlled electric dipole orientation (orthogonal to the sample plane) of the STM excitation is best suited to the excitation of TM modes, e.g. surface

Optics EXPRESS

plasmon polaritons, and provides a source of circular surface waves, isotropically propagating away from the excitation point [28].

The main drawbacks of the electrical excitation of optical modes using the STM are the weakness of the resulting optical signal and the difficulty of detecting TE and nonradiative modes. Nonetheless, these issues could be overcome by implementing various strategies, e.g., based on the engineering of the tip.

Finally, we anticipate that the STM-based technique introduced in this article may be applied to a number of different fields, including, among many others, the characterization of optical modes in nanoresonators, stacked nanoantennas [68], and multilayer stacks incorporating semiconductors [69]. Combining our technique with polarimetry would lead to the characterization of the optical response of chiral nano and microstructures [70]. Beyond optical mode characterization, our technique may be used as an interferometric tool to determine the phase in the optical response of nanostructures, as introduced in [42]. It is also a valuable tool for the testing and design of integrated plasmonic microstructures in view of their integration in optoelectronic microdevices, as proposed in [44]. Finally, a recent report of time-correlated photon pair generation from the tunnel junction of an STM [71] suggests that future experiments in the field of quantum optics are also possible with this technique.

A. Dipole model

As shown in Fig. 2(a), we consider a point-like vertical oscillating electric dipole located at a distance h above the air-metal interface of an Au-SiO_2-Au MIM stack on a glass substrate. A detailed derivation can be found in Refs. [29,50,72]. The oscillating dipole emits a spherical wave. To take advantage of the Fresnel formalism at the interface [48–50], we use the Sommerfeld expansion of a spherical wave in terms of plane waves. In cylindrical coordinates (ρ, ϕ, z), the Sommerfeld expansion reads

$$\frac{\exp(i\,k_0\,R_0)}{R_0} = i\int_0^\infty dk_\rho \frac{k_\rho}{k_z} J_0(k_\rho\,\rho)\,\exp(i\,k_z\,|z-h|) \tag{1}$$

where $R_0 = [\rho + (z-h)]^{1/2}$, and J_0 is the zero-order Bessel function of the first kind. $k_0 = \frac{\omega}{c}$, k_ρ is the in-plane component of the wavevector, and $k_z = \sqrt{k_0^2 - k_\rho^2}$ is its out-of-plane component.

Excitation by a vertical dipole restricts the light polarization to p and the following discussion concerns this polarization only. In the time harmonic approximation ($\exp(-i\omega t)$ convention) the energy flux per unit area through the thin film stack in the z direction, where the last medium is the glass, is given by the Poynting vector (see, e.g., [50])

$$S^{\downarrow}_{glass}(k_\rho, z, \omega) = E_{glass\,\rho}\,H^*_{glass\,\phi}. \tag{2}$$

The electromagnetic fields are given by

$$E_{glass\,\rho}(k_\rho,\ z) = \frac{k_\rho^2}{4\,\pi\,\varepsilon_0\,\varepsilon_{air}}\,\frac{k_{z\,glass}}{k_{z\,air}}\,\frac{\varepsilon_{air}}{\varepsilon_{glass}}\,J_0'(k_\rho\,\rho)\,t^{(p)}(\delta)\exp\{i\,[k_{z\,air}h - k_{z\,glass}(z+\delta)]\} \tag{3}$$

$$H^*_{glass\,\phi}(k_\rho,\ z) = -\frac{\omega}{4\,\pi}\,\frac{k_\rho^2}{k_{z\,air}}\,J_0'(k_\rho\,\rho)\,t^{(p)}(\delta)\exp\{i\,[k_{z\,air}h - k_{z\,glass}(z+\delta)]\} \tag{4}$$

where $k_0 = \omega/c$ and ε_0, ε_{air} and ε_{glass} are the vacuum and relative permittivities. k_ρ is the in-plane wavevector and $k_{z\,glass}$ ($k_{z\,air}$) is the out-of-plane wavevector component in the glass (in the air). $t^{(p)}$ is the Fresnel transmission coefficient of the entire stack (see Appendix B) and δ is the MIM stack thickness.

Optics EXPRESS

The emission in the substrate may be split into two parts, often referred to as the *allowed* (S_a) and *forbidden* (S_f) light [50], which correspond to the propagating and evanescent electric field contributions of the dipole to the light emitted in the substrate, respectively. Thus, when $k_\rho \in [0,\ k_0\, n_{air}]$ the Poynting vector in the substrate reads

$$S_a(k_\rho, z, \omega) = \mathrm{Re}\left\{ \frac{k_0^2\, k^*_{z\,glass}}{\omega\, \mu_0\, \mu} \frac{k_\rho^2\, |t^{(p)}_{1m}(k_\rho,\ z)|^2}{|k_{z\,air}|^2} \right\}. \tag{5}$$

The stack has m layers and the total Fresnel transmission coefficient is $t^{(p)}_{1m}$ corresponding to air-Au-SiO_2-Au-Ti-glass. When $k_\rho \in [k_0\, n_{air}, k_0\, n_{glass}]$ one has

$$S_f(k_\rho, z, \omega) = \mathrm{Re}\left\{ \frac{k_0^2\, k^*_{z\,glass}}{\omega\, \mu_0\, \mu} \frac{k_\rho^2\, |t^{(p)}_{m1}(k_\rho,\ z)|^2}{|k_{z\,air}|^2}\ \exp(-2\, k''_{z\,air}\, h) \right\}. \tag{6}$$

In Eq. 6, the total Fresnel transmission coefficient $t^{(p)}_{m1}$ corresponds to a glass-Ti-Au-SiO_2-Au-air stack and $k''_{z\,air}$ is the imaginary part of $k_{z\,air}$. The Poynting vector $S(k_\rho, z, \omega)$ depends on the spatial coordinate z perpendicular to the interface and the derived expression is valid in the far field. One obtains the dispersion graphs of the main text by calculating the transmitted flux on a grid of real in-plane wave vector k_ρ/k_0 and energy $\hbar\omega$.

B. Fresnel coefficients

The Fresnel transmission coefficient $t^{(p)}$ of the multilayer stack is calculated using the transfer matrix $T(\omega)$ algorithm of Abèles-Bethune [51]

$$T(\omega) = M_{m(m-1)}\Phi_{m-1} \ldots\ldots\ldots \Phi_2 M_{21}. \tag{7}$$

where 1 and m are the first and final semi-infinite layers of the stack. M_{jk} and Φ_j are the transfer matrices at the jk interfaces and the plane wave propagation in medium j, respectively:

$$M_{jk} = \frac{1}{t_{jk}} \begin{pmatrix} 1 & r_{jk} \\ r_{jk} & 1 \end{pmatrix} \tag{8}$$

where the Fresnel reflection r_{jk} and transmission t_{jk} coefficients at a particular interface jk are given in the Appendix of [51], and

$$\Phi_j = \begin{pmatrix} \phi_j & 0 \\ 0 & \bar{\phi}_j \end{pmatrix} \tag{9}$$

where $\phi_j = \exp(i\, k_0\, N_j\, d_j)$, with $N_j = n_j \cos\theta_j$ the effective refractive index, d_j the j^{th}-layer thickness and $\bar{\phi}_j$ the complex conjugate. Using the transfer matrix T of Eq. 7, the electric field in the final layer m reads

$$\begin{pmatrix} E^+_m \\ E^-_m \end{pmatrix} = \begin{pmatrix} T_{11} & T_{12} \\ T_{21} & T_{22} \end{pmatrix} \begin{pmatrix} 1 \\ r \end{pmatrix} E_1 \tag{10}$$

where r is the total Fresnel reflection coefficient including the reflections at all interfaces and E^+_m and E^-_m are the incident and reflected electric fields. In the final layer, the reflected field E^-_m is

Optics EXPRESS

absent and one has

$$E_m^- = 0 = T_{21} + T_{22} r. \tag{11}$$

From this equation one extracts the reflection amplitude r

$$r = \frac{E_1^-}{E_1^+} = \frac{-T_{21}}{T_{22}}. \tag{12}$$

The transmission coefficient is defined as a ratio of the final E_m^+ over the initial E_1^+ amplitude. Since the amplitude $E_1^+ = 1$, one obtains

$$t = \frac{E_m^+}{E_1^+} = T_{11} + r\,T_{12} = T_{11} - \frac{T_{12}T_{21}}{T_{22}}. \tag{13}$$

C. Mode analysis

A calculation of the electric field profile $E(z)$ may be used to identify the nature of a mode in a thin film stack having m interfaces [55,73,74]. To do this, plane wave illumination of the structure from the glass substrate is considered. Thus, using Eq. 6 and the transfer matrix algorithm, one obtains

$$\begin{aligned}
E_1(z) &= \begin{pmatrix} E_1^+ \\ E_1^- \end{pmatrix} = \begin{pmatrix} 1 \\ r \end{pmatrix} E_0 \\
E_2(z) &= \begin{pmatrix} e^{i\,k_{2z}\,(z-z_1)} & 0 \\ 0 & e^{-i\,k_{2z}\,(z-z_1)} \end{pmatrix} \cdot M_{21} \cdot E_1(z_1) && z \in [z_1, z_2] \\
E_j(z) &= \begin{pmatrix} e^{i\,k_{jz}\,(z-z_{j-1})} & 0 \\ 0 & e^{-i\,k_{jz}\,(z-z_{j-1})} \end{pmatrix} \cdot M_{jj-1} \cdot \Phi_{j-1} \cdot E_{j-1}(z_{j-1}) && z \in [z_{j-1}, z_j] \\
E_m(z) &= \begin{pmatrix} e^{i\,k_{mz}\,(z-z_{m-1})} & 0 \\ 0 & e^{-i\,k_{mz}\,(z-z_{m-1})} \end{pmatrix} \cdot M_{m(m-1)} \cdot \Phi_{m-1} \cdot E_{m-1}(z_{m-1}) && z \in [z_{m-1}, z_m]
\end{aligned} \tag{14}$$

where r is the total Fresnel reflection coefficient including all reflections given in Eq. 12. M_{ij} is the interface transfer matrix and Φ_j is the propagation matrix in the j^{th} layer as given in Eqs. 8 and 9 above. $E_j(z)$ is a column vector representing the electric field in the layer j with the components $E_j^+(z)$ and $E_j^-(z)$. The incident $E_j^+(z)$ and reflected $E_j^-(z)$ components are added together to produce the graphs of the electric field as a function of z in Fig. 4.

Funding

China Scholarship Council (201304910386).

Acknowledgments

We acknowledge technical support from the micro-nanotechnology platform of the Center for Nanosciences and Nanotechnologies (C2N-CTU) in Orsay, France, and financial support from the Région Ile-de-France (DIM Nano-K). The financial support of the China Scholarship Council (CSC) (No. 201304910386) and the Alumni Association of the Lebanese University's Faculty of Sciences (Tripoli, Lebanon) is gratefully acknowledged. All fabrication and ellipsometry measurements have been carried out at the micro-nanotechnology platform of the C2N-CTU laboratory in Orsay. S. Cao and M. Achlan contributed equally to this work.

Optics EXPRESS

References

1. T.-H. Lan, Y.-K. Chung, J.-E. Li, and C.-H. Tien, "Plasmonic rainbow rings induced by white radial polarization," Opt. Lett. **37**(7), 1205–1207 (2012).
2. N. Fang, H. Lee, C. Sun, and X. Zhang, "Sub-diffraction-limited optical imaging with a silver superlens," Science **308**(5721), 534–537 (2005).
3. Y. Xiong, Z. Liu, C. Sun, and X. Zhang, "Two-dimensional imaging by far-field superlens at visible wavelengths," Nano Lett. **7**(11), 3360–3365 (2007).
4. S. Dutta Choudhury, R. Badugu, and J. R. Lakowicz, "Directing fluorescence with plasmonic and photonic structures," Acc. Chem. Res. **48**(8), 2171–2180 (2015).
5. J. A. Dionne, E. Verhagen, A. Polman, and H. A. Atwater, "Are negative index materials achievable with surface plasmon waveguides? A case study of three plasmonic geometries," Opt. Express **16**(23), 19001–19017 (2008).
6. E. Verhagen, J. A. Dionne, L. K. Kuipers, H. A. Atwater, and A. Polman, "Near-field visualization of strongly confined surface plasmon polaritons in metal-insulator-metal waveguides," Nano Lett. **8**(9), 2925–2929 (2008).
7. G. Adamo, K. MacDonald, Y. Fu, C.-M. Wang, D. Tsai, F. García de Abajo, and N. Zheludev, "Light Well: A Tunable Free-Electron Light Source on a Chip," Phys. Rev. Lett. **103**(11), 113901 (2009).
8. F. Feng, C. Symonds, C. Schwob, J. Bellessa, A. Maître, J.-P. Hugonin, and L. Coolen, "Active control of radiation beaming from tamm nanostructures by optical microscopy," New J. Phys. **20**(3), 033020 (2018).
9. E. Kretschmann and H. Raether, "Radiative decay of nonradiative surface plasmons excited by light," Z. Naturforsch. A **23**(12), 2135–2136 (1968).
10. H. Kano, S. Mizuguchi, and S. Kawata, "Excitation of surface-plasmon polaritons by a focused laser beam," J. Opt. Soc. Am. B **15**(4), 1381–1386 (1998).
11. A. Bouhelier and G. P. Wiederrecht, "Excitation of broadband surface plasmon polaritons: Plasmonic continuum spectroscopy," Phys. Rev. B **71**(19), 195406 (2005).
12. B. Hecht, H. Bielefeldt, L. Novotny, Y. Inouye, and D. W. Pohl, "Local excitation, scattering, and interference of surface plasmons," Phys. Rev. Lett. **77**(9), 1889–1892 (1996).
13. L. Lalouat, B. Cluzel, F. de Fornel, P. Velha, P. Lalanne, D. Peyrade, E. Picard, T. Charvolin, and E. Hadji, "Subwavelength imaging of light confinement in high-Q/small-V photonic crystal nanocavity," Appl. Phys. Lett. **92**(11), 111111 (2008).
14. L. Lalouat, B. Cluzel, C. Dumas, L. Salomon, and F. de Fornel, "Imaging photoexcited optical modes in photonic-crystal cavities with a near-field probe," Phys. Rev. B **83**(11), 115326 (2011).
15. J. Dellinger, K. Van Do, X. Le Roux, F. de Fornel, E. Cassan, and B. Cluzel, "Hyperspectral optical near-field imaging: Looking graded photonic crystals and photonic metamaterials in color," Appl. Phys. Lett. **101**(14), 141108 (2012).
16. S. Jäger, A. M. Kern, M. Hentschel, R. Jäger, K. Braun, D. Zhang, H. Giessen, and A. J. Meixner, "Au nanotip as luminescent near-field probe," Nano Lett. **13**(8), 3566–3570 (2013).
17. A. W. Schell, P. Engel, J. F. M. Werra, C. Wolff, K. Busch, and O. Benson, "Scanning Single Quantum Emitter Fluorescence Lifetime Imaging: Quantitative Analysis of the Local Density of Photonic States," Nano Lett. **14**(5), 2623–2627 (2014).
18. D. Cao, A. Cazé, M. Calabrese, R. Pierrat, N. Bardou, S. Collin, R. Carminati, V. Krachmalnicoff, and Y. De Wilde, "Mapping the radiative and the apparent nonradiative local density of states in the near field of a metallic nanoantenna," ACS Photonics **2**(2), 189–193 (2015).
19. F. T. Rabouw, P. T. Prins, and D. J. Norris, "Europium-doped $NaYF_4$ nanocrystals as probes for the electric and magnetic local density of optical states throughout the visible spectral range," Nano Lett. **16**(11), 7254–7260 (2016).
20. R. Salas-Montiel, M. Berthel, J. Beltran-Madrigal, S. Huant, A. Drezet, and S. Blaize, "Local density of electromagnetic states in plasmonic nanotapers: spatial resolution limits with nitrogen-vacancy centers in diamond nanospheres," Nanotechnology **28**(20), 205207 (2017).
21. T. Coenen, E. J. R. Vesseur, and A. Polman, "Angle-resolved cathodoluminescence spectroscopy," Appl. Phys. Lett. **99**(14), 143103 (2011).
22. M. Kociak and O. Stéphan, "Mapping plasmons at the nanometer scale in an electron microscope," Chem. Soc. Rev. **43**(11), 3865 (2014).
23. F. J. García de Abajo, "Optical excitations in electron microscopy," Rev. Mod. Phys. **82**(1), 209–275 (2010).
24. E. J. R. Vesseur, T. Coenen, H. Caglayan, N. Engheta, and A. Polman, "Experimental Verification of n=0 Structures for Visible Light," Phys. Rev. Lett. **110**(1), 013902 (2013).
25. A. Mohtashami, T. Coenen, A. Antoncecchi, A. Polman, and A. F. Koenderink, "Nanoscale Excitation Mapping of Plasmonic Patch Antennas," ACS Photonics **1**(11), 1134–1143 (2014).
26. J. Lambe and S. L. McCarthy, "Light emission from inelastic electron tunneling," Phys. Rev. Lett. **37**(14), 923–925 (1976).
27. R. W. Rendell and D. J. Scalapino, "Surface plasmons confined by microstructures on tunnel junctions," Phys. Rev. B **24**(6), 3276–3294 (1981).
28. T. Wang, E. Boer-Duchemin, Y. Zhang, G. Comtet, and G. Dujardin, "Excitation of propagating surface plasmons with a scanning tunnelling microscope," Nanotechnology **22**(17), 175201 (2011).
29. P. Bharadwaj, A. Bouhelier, and L. Novotny, "Electrical Excitation of Surface Plasmons," Phys. Rev. Lett. **106**(22), 226802 (2011).

Optics EXPRESS

30. B. Rogez, S. Cao, G. Dujardin, G. Comtet, E. L. Moal, A. Mayne, and E. Boer-Duchemin, "The mechanism of light emission from a scanning tunnelling microscope operating in air," Nanotechnology **27**(46), 465201 (2016).
31. E. Le Moal, S. Marguet, B. Rogez, S. Mukherjee, P. Dos Santos, E. Boer-Duchemin, G. Comtet, and G. Dujardin, "An electrically excited nanoscale light source with active angular control of the emitted light," Nano Lett. **13**(9), 4198–4205 (2013).
32. P. Johansson, "Light emission from a scanning tunneling microscope: Fully retarded calculation," Phys. Rev. B **58**(16), 10823–10834 (1998).
33. T. Wang, E. Boer-Duchemin, G. Comtet, E. Le Moal, G. Dujardin, A. Drezet, and S. Huant, "Plasmon scattering from holes: from single hole scattering to Young's experiment," Nanotechnology **25**(12), 125202 (2014).
34. E. Le Moal, S. Marguet, D. Canneson, B. Rogez, E. Boer-Duchemin, G. Dujardin, T. V. Teperik, D.-C. Marinica, and A. G. Borisov, "Engineering the emission of light from a scanning tunneling microscope using the plasmonic modes of a nanoparticle," Phys. Rev. B **93**(3), 035418 (2016).
35. M. J. Romero, J. van de Lagemaat, G. Rumbles, and M. M. Al-Jassim, "Plasmon excitations in scanning tunneling microscopy: Simultaneous imaging of modes with different localizations coupled at the tip," Appl. Phys. Lett. **90**(19), 193109 (2007).
36. Y. Zhang, E. Boer-Duchemin, T. Wang, B. Rogez, G. Comtet, E. Le Moal, G. Dujardin, A. Hohenau, C. Gruber, and J. R. Krenn, "Edge scattering of surface plasmons excited by scanning tunneling microscopy," Opt. Express **21**(12), 13938 (2013).
37. S. Divitt, P. Bharadwaj, and L. Novotny, "The role of gap plasmons in light emission from tunnel junctions," Opt. Express **21**(22), 27452–27459 (2013).
38. T. Wang, G. Comtet, E. Le Moal, G. Dujardin, A. Drezet, S. Huant, and E. Boer-Duchemin, "Temporal coherence of propagating surface plasmons," Opt. Lett. **39**(23), 6679–6682 (2014).
39. S. Cao, E. Le Moal, E. Boer-Duchemin, G. Dujardin, A. Drezet, and S. Huant, "Cylindrical vector beams of light from an electrically excited plasmonic lens," Appl. Phys. Lett. **105**(11), 111103 (2014).
40. Z. Dong, H.-S. Chu, D. Zhu, W. Du, Y. A. Akimov, W. P. Goh, T. Wang, K. E. J. Goh, C. Troadec, C. A. Nijhuis, and J. K. W. Yang, "Electrically-excited surface plasmon polaritons with directionality control," ACS Photonics **2**(3), 385–391 (2015).
41. B. Rogez, R. Horeis, E. Le Moal, J. Christoffers, K. Al-Shamery, G. Dujardin, and E. Boer-Duchemin, "Optical and electrical excitation of hybrid guided modes in an organic nanofiber - gold film system," J. Phys. Chem. C **119**(38), 22217–22224 (2015).
42. T. Wang, B. Rogez, G. Comtet, E. Le Moal, W. Abidi, H. Remita, G. Dujardin, and E. Boer-Duchemin, "Scattering of electrically excited surface plasmon polaritons by gold nanoparticles studied by optical interferometry with a scanning tunneling microscope," Phys. Rev. B **92**(4), 045438 (2015).
43. D. Canneson, E. Le Moal, S. Cao, X. Quélin, H. Dallaporta, G. Dujardin, and E. Boer-Duchemin, "Surface plasmon polariton beams from an electrically excited plasmonic crystal," Opt. Express **24**(23), 26186–26200 (2016).
44. S. Cao, E. Le Moal, F. Bigourdan, J.-P. Hugonin, J.-J. Greffet, A. Drezet, S. Huant, G. Dujardin, and E. Boer-Duchemin, "Revealing the spectral response of a plasmonic lens using low-energy electrons," Phys. Rev. B **96**(11), 115419 (2017).
45. S. Cao, E. Le Moal, Q. Jiang, A. Drezet, S. Huant, J.-P. Hugonin, G. Dujardin, and E. Boer-Duchemin, "Directional light beams by design from electrically driven elliptical slit antennas," Beilstein J. Nanotechnol. **9**, 2361–2371 (2018).
46. A. Drezet, A. Hohenau, D. Koller, A. Stepanov, H. Ditlbacher, B. Steinberger, F. Aussenegg, A. Leitner, and J. Krenn, "Leakage radiation microscopy of surface plasmon polaritons," Mater. Sci. Eng., B **149**(3), 220–229 (2008).
47. J.-F. Bryche, G. Barbillon, B. Bartenlian, G. Dujardin, E. Boer-Duchemin, and E. Le Moal, "k-space optical microscopy of nanoparticle arrays: Opportunities and artifacts," J. Appl. Phys. **124**(4), 043102 (2018).
48. W. Lukosz and R. E. Kunz, "Light emission by magnetic and electric dipoles close to a plane interface. I. total radiated power," J. Opt. Soc. Am. **67**(12), 1607–1615 (1977).
49. R. R. Chance, A. Prock, and R. Silbey, *Molecular Fluorescence and Energy Transfer Near Interfaces* (John Wiley & Sons, Inc., 1978), pp. 1–65.
50. L. Novotny, "Allowed and forbidden light in near-field optics. I. a single dipolar light source," J. Opt. Soc. Am. A **14**(1), 91–104 (1997).
51. D. S. Bethune, "Optical harmonic generation and mixing in multilayer media: analysis using optical transfer matrix techniques," J. Opt. Soc. Am. B **6**(5), 910–916 (1989).
52. J. Mooney and P. Kambhampati, "Get the basics right: Jacobian conversion of wavelength and energy scales for quantitative analysis of emission spectra," J. Phys. Chem. Lett. **4**(19), 3316–3318 (2013).
53. J. Mooney and P. Kambhampati, "Correction to "get the basics right: Jacobian conversion of wavelength and energy scales for quantitative analysis of emission spectra"," J. Phys. Chem. Lett. **5**(20), 3497 (2014).
54. P. Törmä and W. L. Barnes, "Strong coupling between surface plasmon polaritons and emitters: a review," Rep. Prog. Phys. **78**(1), 013901 (2015).
55. J. A. Dionne, L. A. Sweatlock, H. A. Atwater, and A. Polman, "Planar metal plasmon waveguides: frequency-dependent dispersion, propagation, localization, and loss beyond the free electron model," Phys. Rev. B **72**(7), 075405 (2005).
56. L. H. Smith, M. C. Taylor, I. R. Hooper, and W. L. Barnes, "Field profiles of coupled surface plasmon-polaritons," J. Mod. Opt. **55**(18), 2929–2943 (2008).

Optics EXPRESS

57. J. Chen, G. A. Smolyakov, S. R. J. Brueck, and K. J. Malloy, "Surface plasmon modes of finite, planar, metal-insulator-metal plasmonic waveguides," Opt. Express **16**(19), 14902–14909 (2008).
58. H. Ditlbacher, N. Galler, D. Koller, A. Hohenau, A. Leitner, F. Aussenegg, and J. Krenn, "Coupling dielectric waveguide modes to surface plasmon polaritons," Opt. Express **16**(14), 10455–10464 (2008).
59. D. Brissinger, L. Salomon, and F. D. Fornel, "Unguided plasmon-mode resonance in optically excited thin film: exact modal description of Kretschmann-Raether experiment," J. Opt. Soc. Am. B **30**(2), 333–337 (2013).
60. Y. Akimov, M. E. Pam, and S. Sun, "Kretschmann-Raether configuration: Revision of the theory of resonant interaction," Phys. Rev. B **96**(15), 155433 (2017).
61. Y. Akimov, "Optical resonances in Kretschmann and Otto configurations," Opt. Lett. **43**(6), 1195–1198 (2018).
62. A. P. Vinogradov, A. V. Dorofeenko, A. A. Pukhov, and A. A. Lisyansky, "Exciting surface plasmon polaritons in the Kretschmann configuration by a light beam," Phys. Rev. B **97**(23), 235407 (2018).
63. F. Bigourdan, J.-P. Hugonin, F. Marquier, C. Sauvan, and J.-J. Greffet, "Nanoantenna for electrical generation of surface plasmon polaritons," Phys. Rev. Lett. **116**(10), 106803 (2016).
64. S. Le Liepvre, P. Du, D. Kreher, F. Mathevet, A.-J. Attias, C. Fiorini-Debuisschert, L. Douillard, and F. Charra, "Fluorescent Self-Assembled Molecular Monolayer on Graphene," ACS Photonics **3**(12), 2291–2296 (2016).
65. R. M. Bakker, V. P. Drachev, H.-K. Yuan, and V. M. Shalaev, "Near-field, broadband optical spectroscopy of metamaterials," Phys. B (Amsterdam, Neth.) **394**(2), 137–140 (2007).
66. P. Dvořák, Z. Édes, M. Kvapil, T. Šamořil, F. Ligmajer, M. Hrtoň, R. Kalousek, V. Křápek, P. Dub, J. Spousta, P. Varga, and T. Šikola, "Imaging of near-field interference patterns by aperture-type SNOM – influence of illumination wavelength and polarization state," Opt. Express **25**(14), 16560–16573 (2017).
67. M. G. Boyle, J. Mitra, and P. Dawson, "Infrared emission from tunneling electrons: The end of the rainbow in scanning tunneling microscopy," Appl. Phys. Lett. **94**(23), 233118 (2009).
68. R. Esteban, T. V. Teperik, and J. J. Greffet, "Optical Patch Antennas for Single Photon Emission Using Surface Plasmon Resonances," Phys. Rev. Lett. **104**(2), 026802 (2010).
69. C. Symonds, A. Lemaître, E. Homeyer, J. C. Plenet, and J. Bellessa, "Emission of Tamm plasmon/exciton polaritons," Appl. Phys. Lett. **95**(15), 151114 (2009).
70. Y. Gorodetski, A. Drezet, C. Genet, and T. W. Ebbesen, "Generating Far-Field Orbital Angular Momenta from Near-Field Optical Chirality," Phys. Rev. Lett. **110**(20), 203906 (2013).
71. C. C. Leon, A. Rosławska, A. Grewal, O. Gunnarsson, K. Kuhnke, and K. Kern, "Photon superbunching from a generic tunnel junction," Sci. Adv. **5**(5), eaav4986 (2019).
72. L. Novotny and B. Hecht, *Principles of nano-optics* (Cambridge University, 2012).
73. J. A. Dionne, L. A. Sweatlock, H. A. Atwater, and A. Polman, "Plasmon slot waveguides: Towards chip-scale propagation with subwavelength-scale localization," Phys. Rev. B **73**(3), 035407 (2006).
74. S. Refki, S. Hayashi, A. Rahmouni, D. Nesterenko, and Z. Sekkat, "Anticrossing behaviour of surface plasmon polariton dispersions in metal-insulator-metal structures," Plasmonics **11**(2), 433–440 (2016).